Microstructural evolutions and impact toughness in simulated welding heat affected zones for a high-strength carbide-free bainitic rail steel

Bai, Wei; Xu, Xiaojun; Liu, Yaolan; Liang, Yunxiao; Shen, Yijie; Han, Zhenyu; Sheng, Zhendong; Chen, Rong; Zhu, Minhao

DOI
10.1016/j.msea.2023.145325

Publication date
2023

Document Version
Final published version

Published in
Materials Science and Engineering: A

Citation (APA)
Bai, W., Xu, X., Liu, Y., Liang, Y., Shen, Y., Han, Z., Sheng, Z., Chen, R., & Zhu, M. (2023). Microstructural evolutions and impact toughness in simulated welding heat affected zones for a high-strength carbide-free bainitic rail steel. *Materials Science and Engineering: A*, *880*, Article 145325. https://doi.org/10.1016/j.msea.2023.145325

Materials Science & Engineering A 880 (2023) 145325

Contents lists available at ScienceDirect

Materials Science & Engineering A

journal homepage: www.elsevier.com/locate/msea

Microstructural evolutions and impact toughness in simulated welding heat affected zones for a high-strength carbide-free bainitic rail steel

Wei Bai [a,b], Xiaojun Xu [a,c,*], Yaolan Liu [a], Yunxiao Liang [a], Yijie Shen [a], Zhenyu Han [b], Zhendong Sheng [b], Rong Chen [b], Minhao Zhu [a]

[a] Key Laboratory of Advanced Technologies of Materials (Ministry of Education), School of Materials Science and Engineering, Southwest Jiaotong University, Chengdu, 610031, PR China

[b] Pangang Group Research Institute Co., Ltd, State Key Laboratory of Vanadium and Titanium Resources Comprehensive Utilization, Panzhihua, Sichuan, 617000, PR China

[c] Novel Aerospace Materials Group, Faculty of Aerospace Engineering, Delft University of Technology, 2629HS, Delft, the Netherlands

ARTICLE INFO

Keywords:
Bainitic rail steel
Welding thermal simulation
Peak temperature
Microstructural evolutions
Impact toughness

ABSTRACT

Systematic experimental investigations were conducted to study the microstructures and impact toughness of each heat affected zone (HAZ) formed during rail flash-butt welding. A high-strength carbide-free bainitic rail steel was subjected to different thermal simulation cycles to separately reproduce each HAZ subzone by tailoring the peak temperature (PT) with respect to 700, 850, 920, 1000 and 1350 °C, and hence to generate the corresponding microstructures by using Gleeble-3500 simulator. Results show that the HAZ subzones exhibit complicated microstructures depending on the PTs, and with increasing PT the dominant bainitic microstructure type evolves from polygonal bainitic ferrite (700 °C) to a mixture of fine bainitic ferrite and granular bainite (850–1000 °C), and finally to coarse bainitic ferrite and granular bainite (1350 °C). Impact tests demonstrate that the impact toughness initially increases significantly as the PT reaches 920 °C (i.e., fine-grained HAZ), beyond which the impact toughness starts to decrease. The fine-grained HAZ displays optimal impact toughness in HAZs, yet which is lower than the base metal. Moreover, the morphology and distribution of martensite-austenite (M-A) constituents is strongly dependent on the welding PT, and the high fraction blocky and coarse slender M-A constituents is considered to be detrimental for the impact toughness.

1. Introduction

With the rapid development of railway industry orienting towards high-speed and heavy-haul, the service conditions of rails become increasingly harsher, consequently resulting in high requirements on the strength, wear resistance and fatigue resistance for rail materials. At present, the rail materials are mainly eutectoid and hypereutectoid steels consisting of a dominant pearlitic structure. With the aid of microalloying [1], heat treatment [2,3] and thermal mechanical control processing (TMCP) technology [4], the ultimate tensile strength (UTS) of premium pearlitic rail has exceeded 1450 MPa [5]. Nonetheless, for the pearlitic rails it is significantly difficult to further improve the service performance to meet the harsh conditions by means of the methods above. Moreover, the toughness, ductility and rolling contact fatigue (RCF) resistance of pearlitic rails still remain at a relative low level, which can hardly satisfy the high demands of railway transport with a greater traffic density, higher axle load and heavier total freight volume [6]. In order to prolong the life time of railways, numerous studies [2,7,8] have been carried out to seek alternatives to upgrade rail materials. Considering the promising strength and toughness combination, the carbide-free bainitic (CFB) rails have received a lot of attention in the academic fields and industries, and are expected to become a new generation of rails [9–11].

Over the past decades, significant progress has been made on the base material of CFB rails, such as industrial production [11], wear and contact fatigue damage [12–15], ratchetting-fatigue interaction [16] and hydrogen embrittlement behavior [17,18]. Nevertheless, given that rail welding is the principal method to realize seamless railway which can greatly improves the running speed, stability and riding comfort of trains [19], the service performance of welded joints of bainitic rails as

* Corresponding author. Key Laboratory of Advanced Technologies of Materials (Ministry of Education), School of Materials Science and Engineering, Southwest Jiaotong University, Chengdu, 610031, China, PR China.
E-mail addresses: xiaojunxu0617@126.com, xiaojunxu@swjtu.edu.cn (X. Xu).

https://doi.org/10.1016/j.msea.2023.145325
Received 5 May 2023; Received in revised form 16 June 2023; Accepted 17 June 2023
Available online 18 June 2023

the weak area of the whole track structure remains a challenge. Compared to the commonly used rail welding technologies [20–22], flash-butt welding (FBW) has the advantage of reliable welding quality and high productivity over thermite and gas pressure welding, and hence has become the mainstream method to produce seamless railways. However, upon welding, the microstructure of joint will differ from the parent microstructure due to the formation of heat affected zone (HAZ), which will degrade the mechanical properties of joint. In general, the HAZs can be classified into four types of subzones based on the peak temperature (PT) during single-cycle welding and the austenite starting (Ac_1) and finishing (Ac_3) temperature [23,24]: (i) coarse-grained HAZ (CGHAZ), where austenite grain grows seriously and the PT reaches up to 1300 °C above; (ii) fine-grained HAZ (FGHAZ), where the PT is above the Ac_3 (i.e., Ac_3~1100 °C) and austenite grain growth depends on specific PT and duration at high temperature; (iii) intercritical HAZ (ICHAZ), where the PT is within the Ac_1~Ac_3, accompanying by incomplete austenitization and insufficient transformation during cooling; (iv) subcritical HAZ (SCHAZ), where the PT is lower than the Ac_1 while over-tempering occurs. As reported previously [25–28], the welding PT is one of the most critical parameters in determining the mechanical properties of welded alloyed steels, especially for the impact toughness. Di et al. [25] pointed the martensite transformed from reverted austenite upon the welding PT was primarily responsible for the low crack initiation energy in ICHAZ. Li et al. [26] reported the welding PT influence the austenite grain size in CGHAZ, which subsequently varied the martensite-austenite (M-A) constituent morphology and hence the impact toughness. Hu et al. [27] suggested the nanoscale (Ti, Mo)C precipitates in HAZs firstly coarsened and then dissolved as increasing welding PT, leading to a significant variation in mechanical properties. Rios et al. [28] found the welding PT is related to the austenitization and homogenization of alloying elements (particularly C), which further affects the austenite content in HAZs. Moreover, Poorhaydari et al. [29] pointed the ununiform microstructure distribution in joints for single-cycle welding was mainly due to the varied PT in each HAZ subzone, but was less irrelevant to corresponding cooling rate since the little differences among them. While these studies certainly clarified some issues, in these studies either the microstructure of joints were examined for one specific subzone or the impact toughness of each HAZ subzone was not well separated from that of joints. Systematic investigations into the microstructure and impact toughness in different HAZ subzones of welded joint of bainitic rail steel are still lacking. Hence, the response of microstructural evolution for each HAZ subzone on impact toughness is still not yet clear.

Given the outstanding issues discussed above, the objective of current work is to clarify the microstructure and resulting impact toughness of each HAZ subzone for a high-strength CFB rail steel. To reveal the impact toughness of each HAZ subzone, welding thermal simulations by using Gleeble-3500 simulator were carried out to separately reproduce the real PT of each subzone, and hence to simulate the corresponding microstructural feature. The correlation between welding PT and microstructural evolution was investigated. The impact toughness of resulting microstructural features for five different HAZ subzones was evaluated by instrumented Charpy impact test. Meanwhile, the fracture morphologies and crack propagation modes were also discussed.

2. Experimental procedures

2.1. Materials

A new low carbon CFB rail steel of 1380 MPa (min. UTS) grade provided by Pangang Group Co., Ltd. (Panzhihua, China) based on online heat-treatment technology [30] was chosen for current study aiming to conduct thermal simulations on different HAZs of rail welded joint. The composition of rail steel was Fe-0.21C-1.8Si-1.5Mn-1.10(Cr + V + Mo) (in wt.%). The addition of high silicon (>1.5 wt%) can effectively suppress carbides precipitation during bainite transformation [31]. Given that tempering can effectively stabilize retained austenite (RA) [32], the raw bainitic rail with 60 kg/m profile was tempered at 350 °C for 4 h to achieve the optimum strength and toughness balance before machining. The tensile and impact properties listed in Table 1 was tested base on TB/T 2344–2020 at ambient temperature (25 °C). The specimens for impact (10 × 10 × 55 mm^3) and dilatometer (Φ4 × 10 mm^2) tests were sampled within 15 mm from rail head tread, located within the hardened layer (~30 mm) of rail head.

2.2. Welding thermal simulation procedures

During a real welding, the temperature distribution of joint continuously varies from weld center to base metal, forming various subzones (i.e., SCHAZ, ICHAZ, FGHAZ and CGHAZ) in HAZ as stated previously. To approach the real rail welding, the data acquisited from flash-butt welding of investigated rail steel were used for thermal simulation procedures determination. The rail welder, thermocouple layout diagram and actual joint for temperature measurement, and thermal cycle curve of weld center are shown in Fig. 1. The data, such as peak temperature, heating and cooling rates, were acquisited by Yokogawa AX110-1-3 contact thermoscope with embedding Pt–30Rh (platinum-30% rhodinum) and Pt–6Rh (platinum-6% rhodium) thermocouples on the lateral rail head of joint, as illustrated in Fig. 1(b–e). To avoid burning loss, the thermocouples were protected by ceramic bushing during the whole welding process. The sketch maps of temperature measurement are shown in Fig. 1(b,d). The Ac_1 and Ac_3, and the bainite starting (B_s) and finishing (B_f) temperatures (seen in Fig. 10b) for HAZs upon different PTs were determined using dilatometric curves tested by DIL 805 dilatometer, as shown in Fig. 2a where the Ac_1 and Ac_3 temperature was identified to be ~769 °C and ~878 °C, respectively.

The heating and cooling rates of thermal simulations refer to the welding thermal cycle curve shown in Fig. 1e. In order to well simulate the temperature states of different HAZs (i.e., SCHAZ, ICHAZ, FGHAZ and CGHAZ), on the basis of the temperature monitoring data, the simulated specimens were heated at 15.0 °C/s to the PT of 700, 850, 920, 1000 and 1350 °C with holding time for 2 s. The subsequent cooling process was carried out following three temperature stages (i.e., PT to 800 °C, 800 to 500 °C and 500 to 200 °C) with corresponding cooling rate of 10.0 °C/s, 1.2 °C/s and 0.3 °C/s, respectively. Accordingly, the PT-700 °C, PT-850 °C and PT-1350 °C refer to the SCHAZ, ICHAZ and CGHAZ, respectively, while the PT-920 °C, PT-1000 °C both correspond to the FGHAZ. The detailed thermal simulation routes and parameters are shown in Fig. 2b.

2.3. Microstructural characterization and mechanical properties test

The diagram for optical microscope (OM), scanning electron microscope (SEM), electron backscatter diffraction (EBSD) and transmission electron microscope (TEM) characterization as well as hardness tests was given in Fig. 3. After wire cutting, the fractured impact specimens were mounted and polished following the standard metallographic preparation, and were chemically etched with 2 vol% Nital solution. The microstructural features and fracture morphologies were examined by SEM + EBSD (Zeiss Sigma 500). The EBSD specimens were prepared by electrochemical polished with 9 vol% perchloric acid alcohol at 32 V and 20 °C, and the data were acquisited at step size of

Table 1
Tensile and impact properties of investigated rail steel.

YS (MPa)	UTS (MPa)	Yield ratio (YS/UTS)	Elongation (%)	Impact energy (CUN,J)
1362.0 ± 7.0	1452.5 ± 3.5	0.94 ± 0.1	15.5 ± 0.7	212.2 ± 5.0

Note: YS—yield strength, 0.2% offset; UTS—ultimate tensile strength; Elongation—elongation after fracture; CUN—Charpy U-notch.

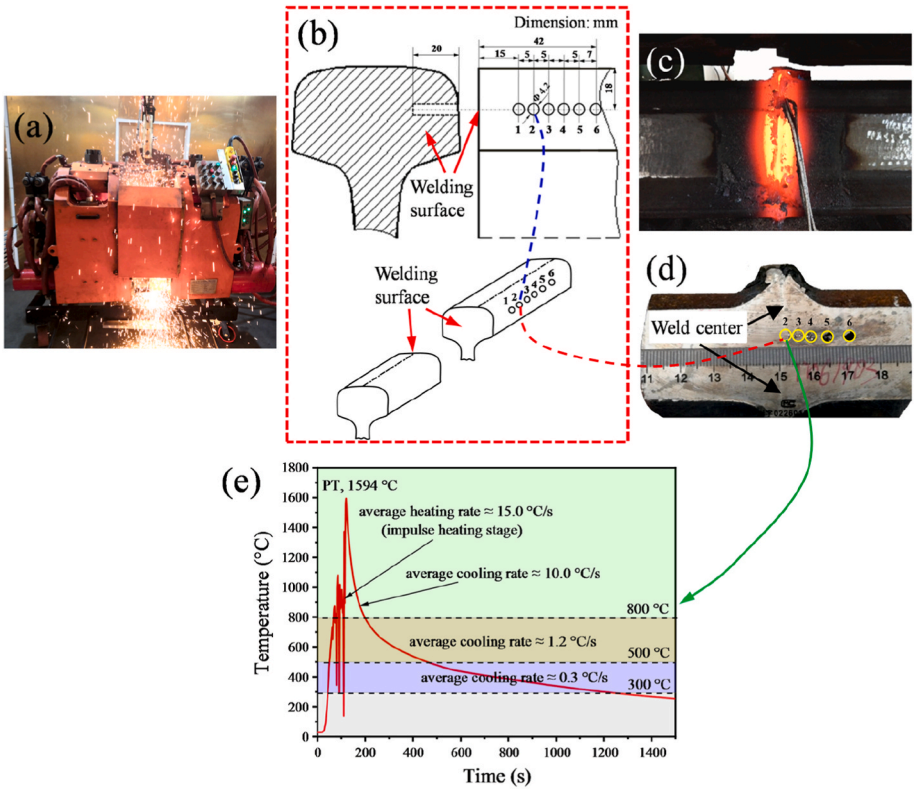

Fig. 1. Temperature monitoring of rail welding: (a) CFB rail welding achieved by YHG-1200 mobile flash-butt welder at heat input of 8.3 MJ; (b) layout diagram of thermocouple embedding in the lateral rail head before welding; (c) temperature measurement after rail welding; (d) longitudinal section of rail joint showing the actual position of thermocouples after welding; (e) thermal cycle curve of weld center corresponding to position '2' shown in Fig. 1(b,d).

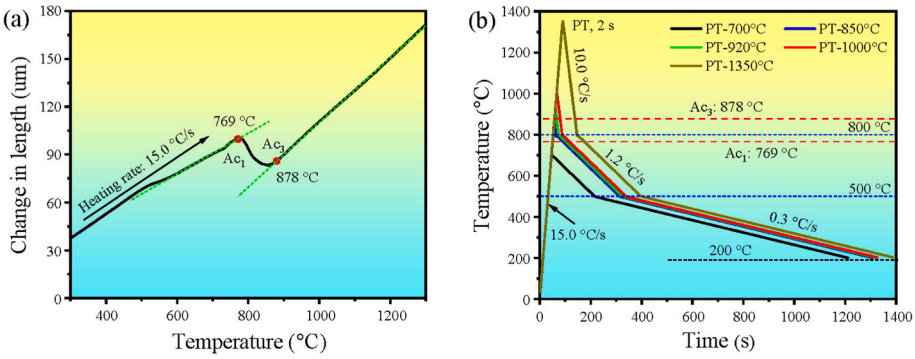

Fig. 2. (a) Dilatometer curve of investigated rail steel at heating rate of 15.0 °C/s; (b) welding thermal cycle curves of simulated HAZs subjected to different PTs.

0.25 μm, while the results were post-processed by HKL Channel 5 software. The intercept methodology was used to measure the prior austenite grain size with average value of 10 measurements based on the SEM images. The macroscopic observation of impact fractures was performed by Leica DFC425 stereomicroscope. Lepera etchant was used to identify the M-A constituents. The metallographic structure was observed by OM (Zeiss Axio Observer.A1m), and the morphological features of M-A constituents were statistical analysis using image-pro plus (IPP) software. Thin foils with a 3 mm diameter for each case were prepared with electrochemically polished in a 5 vol% perchloric acid alcohol at 75 V and −20 °C for microstructure observation by FEI Tecnai G2 F20 TEM. The micro-hardness measurements were carried out using a Vickers indenter (KB30S-FA) at a load force of 1 kgf for holding time of 10 s, and the average value of 10 measurements is reported. Based on GB/T 229–2007, the impact specimens with standard Charpy U-notch (2 mm in notch depth) were used for evaluating the impact toughness via an instrumented impact tester (SANS ZBC2602-D) at ambient temperature (25 °C). Three parallel impact tests were conducted on the base metal (BM) specimens and specimens of each thermal simulation process.

3. Results

3.1. Microstructure observations

In the current study, five thermal simulation specimens subjected to various PTs were produced to represent the typical subzones of welding HAZ. Their microstructures and the BM in the form of OM and SEM micrographs are shown in Fig. 4. As expected, they show diverse microstructural features upon the series of PTs. The BM microstructure (Fig. 4a) is dominated by fine bainitic ferrite (BF) with some filmy retained austenite (RA), M-A constituents, allotriomorphic ferrite (AF)

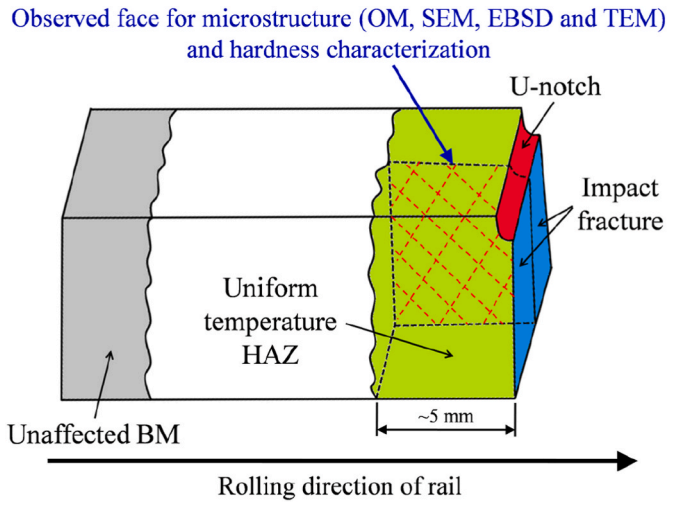

Fig. 3. Testing position diagram of thermal simulation specimen for macroscopic & microscopic characterization. Note: testing position of the BM specimen is consistent with the thermal simulation specimen.

and tempered martensite (TM) with dispersed carbides, accompanied by clear prior austenite grain boundaries (PAGBs). While for PT-700 °C, the fine BF as formed in BM disappears, but an evident polygonal BF and TM is observed instead (Fig. 4b). Combined with the OM image, the carbides (black in color) are prone to be formed along the PAGBs. With the PT increases up to 850, 920 and 1000 °C, a more complicated microstructure consisting of BF, AF, fresh martensite (M), granular bainite (GB) and M-A constituents is observed (Fig. 4(c–e)). Meanwhile, the volume fraction of AF and M decreases continuously as increasing PT, which could be related to the homogenization of austenite. With the increase in PT (austenization temperature), the diffuse of solute atoms (such as C and Mn) becomes more sufficient and then the solute-depleted and solute-rich regions gradually decrease in austenite, which could increase the homogenization of austenite and then inhibit the ferrite (AF) and martensite formation during cooling as stated in Ref. [33]. As a result, it leads to the decrease in the volume fraction of AF and M with the PT raises. As the PT increases to 1350 °C, there are more BF and coarse M-A constituents (Fig. 4f), together with necklace-like M-A constituents formed along the PAGBs which are prone to cause stress concentration and deteriorate the toughness [34]. Furthermore, it is worth noting that the grain size of prior austenite changes depending on the PT. As can be seen, for the BM and PT-700 °C, the prior austenite grain sizes are within 30~40 μm. While for PT-850 °C and PT-920 °C, obvious austenite grain refinement occurs with average size of ~15 μm. As the PT increases to

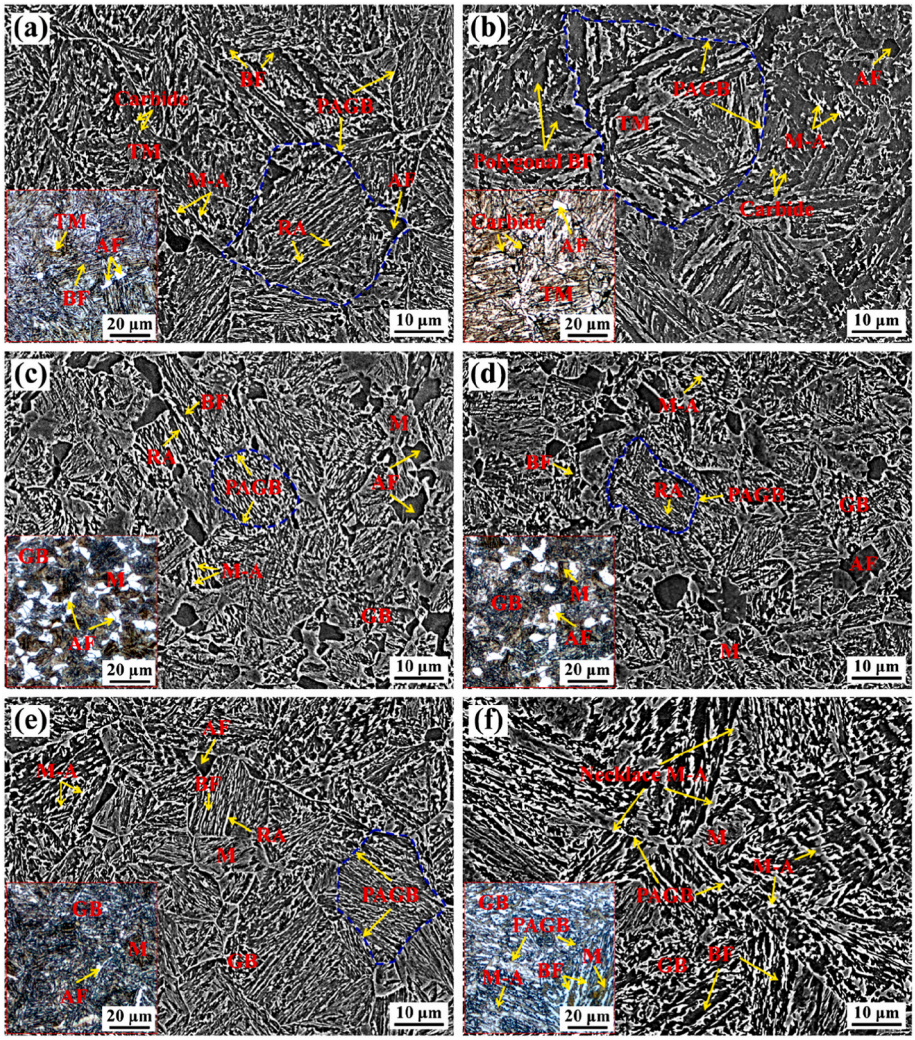

Fig. 4. SEM and corresponding OM (bottom left) images of the microstructures: (a) BM, (b) PT-700 °C, (c) PT-850 °C, (d) PT-920 °C, (e) PT-1000 °C and (f) PT-1350 °C.

1000 °C, the austenite grain size starts to increase to ~30 μm. In particular for the highest PT of 1350 °C, severe austenite grain coarsening occurs with average size of ~100 μm, which could lead to a serious microstructure embrittlement.

In order to deepen the understanding on microstructure observations, Fig. 5 gives the TEM investigation of the microstructures for the BM and thermal simulation specimens. As shown in Fig. 5a, the BM presents fine BF with lath width of ~500 nm. The selected area electron diffraction (SAED) pattern in Fig. 5b confirms the presence of filmy RA, which is located between BF laths and may be contributed to the toughness improvement [32]. Meanwhile, a high density of dislocation (Fig. 5a) and dislocation tangles (Fig. 5c) are observed on BF lath, which could be beneficial to further improve the strength and toughness. While for PT-700 °C, the BF lath experienced the recovery and transformed to polygonal BF (Fig. 5d), consequently leading to nearly free dislocations due to the possibility of continuous slip recombination or cancellation of dislocations [35]. As the PT increases to 850 °C, the polygonization of BF aggravates, and a recovered dislocation substructure and carbides with the size of 50~70 nm are observed (Fig. 5e). SAED pattern in Fig. 5f indicates that the precipitated carbides are Fe_3C with an orthogonal structure, which could be related to the spheroidization of cementite. At the PT of 920 °C, evident BF laths are observed with the width of 600~800 nm (Fig. 5g) but no spheroidized cementite is found as appeared in PT-850 °C. As the PT arises to 1000 °C, the BF tends to be a widened lath (Fig. 5h), and it is worth noting that the fresh BF was transformed from RA in blocky M-A constituent, as marked by red arrows in Fig. 5i. In the case of the highest PT of 1350 °C, the lath width of BF reaches up to 2.0 μm and the M-A constituents distributed between BF laths are in the form of block or film shape (Fig. 5j). Besides, twin martensite appears in the M-A constituent (Fig. 5(k and l)), which could be detrimental to the toughness due to its hard and brittle nature [36].

3.2. EBSD characterization for grain boundary misorientation and retained austenite

In order to further unravel the microstructural evolutions for grain

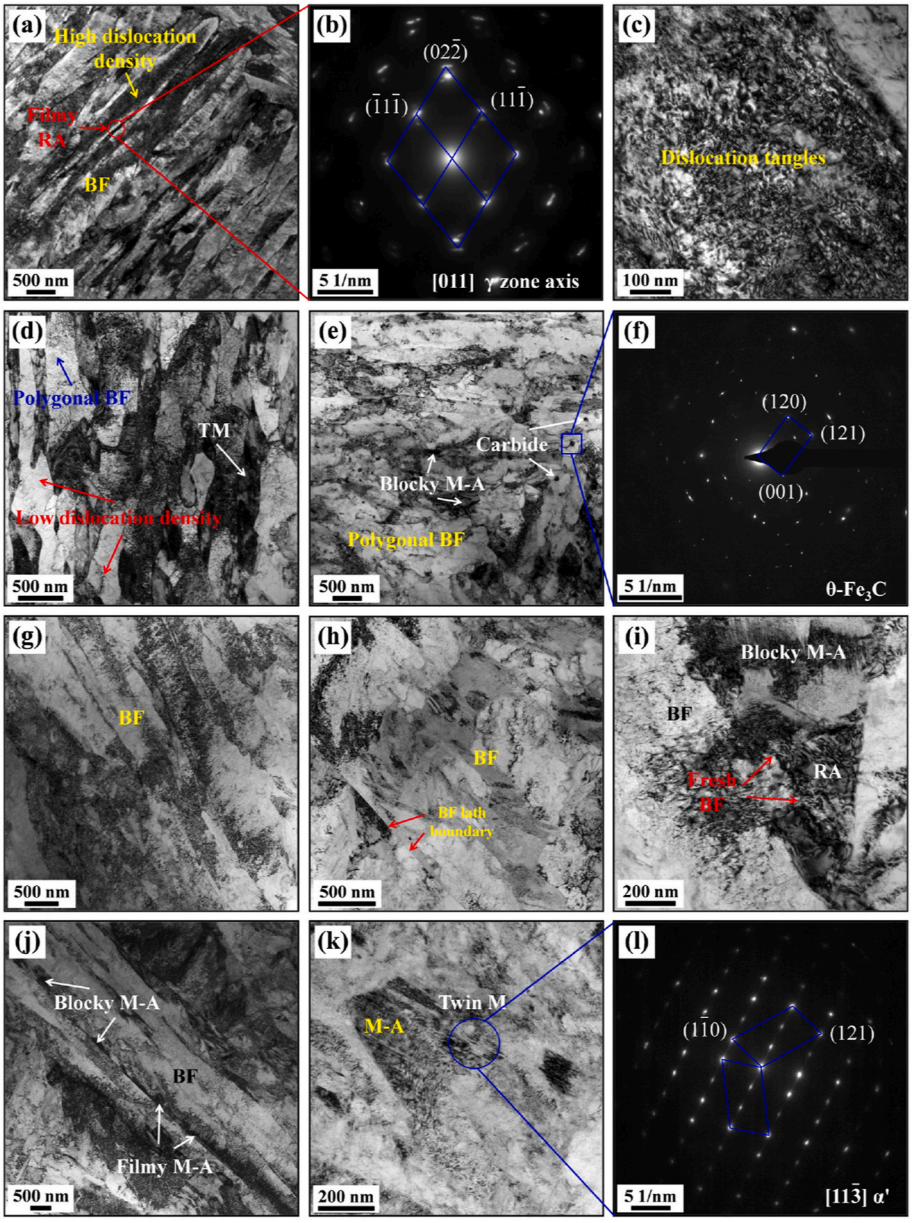

Fig. 5. Bright field TEM images and SAED patterns of the BM and simulated HAZs: (a–c) BM, (d) PT-700 °C, (e–f) PT-850 °C, (g) PT-920 °C, (h–i) PT-1000 °C and (j–l) PT-1350 °C.

boundary and RA before and after simulated thermal cycles, the combined band contrast, grain boundary misorientation and phase maps based on EBSD data are displayed in Fig. 6. In this work, the grain boundary misorientation as indicated in EBSD results are classified with 15° as the boundary [37], i.e., the low angle grain boundaries (LAGBs, $2° < \theta \leq 15°$) and high angle grain boundaries (HAGBs, $\theta > 15°$), which were marked with blue and black lines, respectively. The band contrast maps in combination with phase identification were applied to distinguish phases. It is evident that all the specimens possess a body-centered cubic (BCC) matrix, and the sub-structures (blocks, grey in color) may compose of BF, AF and M. Meanwhile, the content of RA (red in color, face-centered cubic (FCC) structure) in HAZs varies as the PT increases. As shown in Fig. 6a, the BM has a 30% number fraction of HAGBs. As the PT reaches 700 °C, the HAGBs fraction increases to 32% (Fig. 6b) which may be associated with the recovery of BF lath upon heating [38]. As the PT increases to 850 °C, the resulting microstructure has a highest HAGBs fraction (51%), which may be mainly due to the formation of many M blocks and AF (seen in Fig. 4c). As shown in Fig. 6c, the lower band contrast reveals that the dark grey regions involve a high density of defect and dislocation corresponding to the martensite as reported in Refs. [39,40], which hence significantly increase the HAGBs fraction due to its fine-grained structure. As the PT reaches 920 °C, the decrease in fine-grained structure and AF leads to the reduction in HAGBs fraction (Fig. 6d). Similarly, for PT-1000 °C and PT-1350 °C, the HAGBs continue to decrease (Fig. 6(e and f)). The difference is that the PT-1350 °C has a severely coarsened austenite grain boundary with a highest 5% volume fraction of RA, which is distributed along the HAGBs and matrix as marked in red. The highest volume fraction of RA could be the result of the highest level of homogenizaiton of austensite at the PT-1350 °C due to the sufficient diffusion of soulte atoms (C, Mn). Consequently, there are somewhat high amount of austenite retained at the room temperature.

Fig. 7a gives the statistics of misorientation angle distribution and relative fraction of LAGBs ($\theta \leq 15°$) and HAGBs ($\theta > 15°$). It is clear that the HAGBs fraction firstly increases as increasing PT, and gets a critical PT at 850 °C after which the HAGBs fraction starts to decrease, but the opposite holds for the LAGBs, which suggests that there is a highest HAGBs fraction at PT-850 °C. Moreover, as stated in Refs. [41,42], the HAGBs with misorientation angle higher than 45° could effectively hinder or deflect the crack propagation. Therefore, the HAGBs were further divided into two kinds with respect to the benchmark of 45° misorientation angle. As Fig. 7a presents, the PT-850 °C has a highest HAGBs fraction ($\theta > 45°$, 41%), while the PT-1350 °C has a lowest HAGBs fraction ($\theta > 45°$, 22%). Fig. 7b presents the distribution of effective grain size for various BCC phases (i.e., BF, AF and M). The effective grain size is the equivalent size of effective grains which is separated by HAGBs with misorientation angle greater than 15°, as stated in Ref. [43]. As seen, the average effective grain size firstly decreases, and then increases as increasing PT. At the PT-850 °C and PT-920 °C, there is a smallest size of 1.1 μm, which could be mainly attributed to the formation of fine-grained BF (Fig. 4(c and d)) and fine-grained M (Fig. 6(c and d)). In contrast, the relatively large average effective grain size in PT-1000 °C (1.8 μm) and PT-1350 °C (2.1 μm) may be due to high austenitizing temperature, which can promote the growth of BF blocks (Fig. 6(e and f)).

3.3. The hardness and Charpy impact test

The micro-hardness and impact toughness plotted as a function of PT are presented in Fig. 8. Meanwhile, the prior austenite grain sizes upon different PTs are also plotted so as to correlate with the micro-hardness. As seen, with the PT increases, the hardness firstly increases and then decreases, which strongly depends on the nature of microstructures due to the introduced thermal cycles (i.e., PT). It can also be found the hardness trend with PT is opposite to the evolution of prior austenite grain size. A smaller grain size of prior austenite can be observed in PT-850 °C and PT-920 °C for which a higher hardness is obtained. Compared to the HAZs, however, the BM possesses a highest hardness. Fig. 8b gives the impact toughness including the crack initiation energy (CIE) and crack propagation energy (CPE) as a function of PTs. It is clear that both the CIE and CPE follow the same trends as the hardness with increasing PT, i.e., firstly increases and then decreases. As Ref. [44] stated, a fine prior austenite grain size can give rise to dense grain boundary barriers, which consequently elevate the threshold stress intensity and lower the probability of crack evolution. As a result, it can both increase the CIE and CPE as well as the hardness, i.e., the smaller prior austenite grain size, the higher impact toughness and hardness.

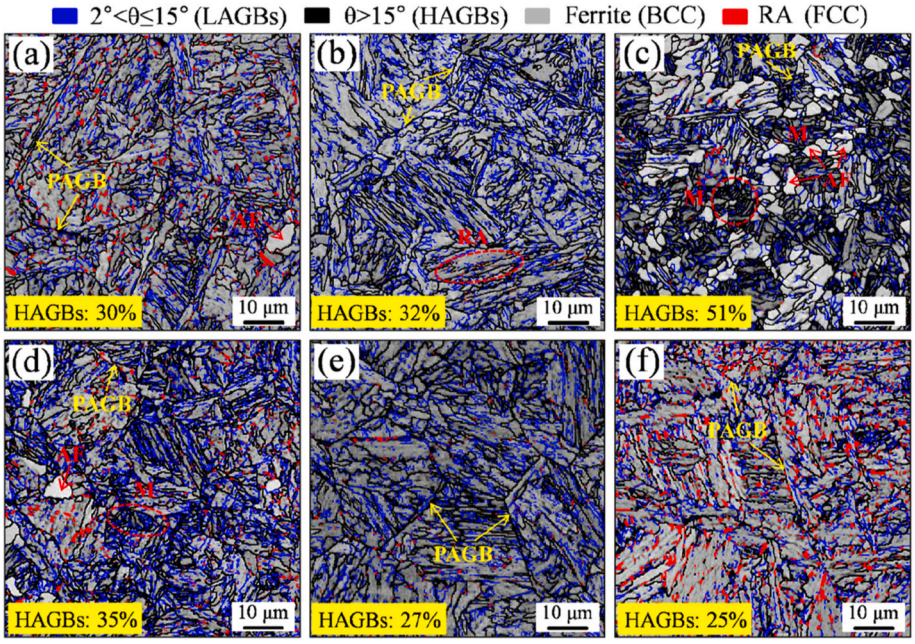

Fig. 6. The combined band contrast, grain boundary misorientation and phase maps: (a) BM, (b) PT-700 °C, (c) PT-850 °C, (d) PT-920 °C, (e) PT-1000 °C and (f) PT-1350 °C.

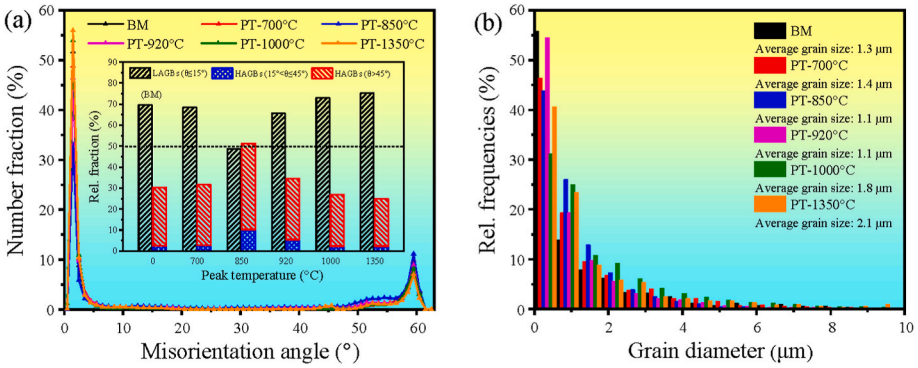

Fig. 7. EBSD results of the BM and simulated HAZs: (a) misorientation angle distribution and relative fraction of LAGBs and HAGBs, (b) the distribution of effective grain size.

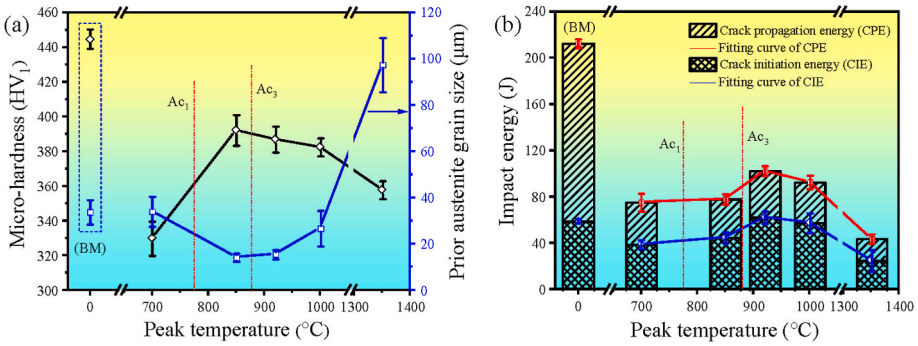

Fig. 8. Micro-hardness and impact toughness of the BM and simulated HAZs: (a) Vickers hardness and prior austenite grain size as a function of PT, (b) impact toughness including the crack initiation and crack propagation energy as a function of PT.

3.4. *Impact fracture morphologies*

Fig. 9 gives the macroscopic morphologies of impact fractures, which were generally divided into three regions, i.e., fibrous (tearing) region, radial region and shear slip. As can be seen, a typical ductile failure can be observed on the fracture face of the BM specimen as shown in Fig. 9a. In contrast, the fracture faces of all HAZ specimens are relatively flat (Fig. 9(b–f)), especailly for PT-1350 °C (Fig. 9f). Furthermore, the

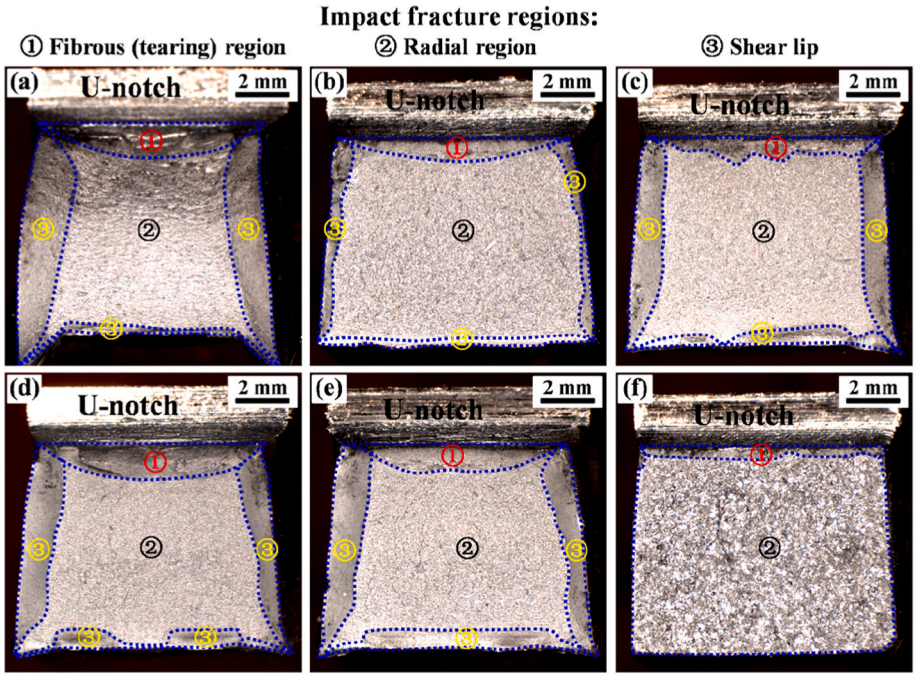

Fig. 9. Macroscopic morphologies of impact fractures by stereomicroscope observations: (a) BM, (b) PT-700 °C, (c) PT-850 °C, (d) PT-920 °C, (e) PT-1000 °C and (f) PT-1350 °C.

fibrous (tearing) regions corresponding to the area where crack initiation appears are evident for all impact specimens. By comparing the area of various fracture regions, the radial region accounts for the majority of each fracture. In order to deepen the observation of main impact fracture behavior, a high-resolution SEM was used to investigate the fracture morphologies as seen in Fig. 10.

Fig. 10 presents the radial region morphologies of impact fractures. The BM has a typical ductile fracture (Fig. 10a), and a large number of dimples with various sizes are observed. While for PT-700 °C, the fracture mechanism is dominated by quasi-cleavage fracture consisting of blunt tearing ridges and tiny cleavage facets (Fig. 10b). The fracture is relatively flat and only some small-size dimples are observed around the tear ridges. In the case of HAZs with PT of 850, 920 and 1000 °C, a mixed ductile and cleavage fracture is observed (Fig. 10(c–e)), and the dimple size seems to grow up as increasing PT. For PT-850 °C (Fig. 10c), the sharpness of tear ridges is more evident than PT-700 °C, suggests that crack propagation becomes difficult and experiences multiple deflections. Besides, the cleavage facet size is relatively large, which may be due to the massive M as observed in Fig. 4c. As the PT reaches 920 °C, the cleavage facet size is relatively small and the fracture morphology mainly presents dimples and ductile tearing ridges with sharp edges (Fig. 10d), which could be beneficial to the toughness. As the PT increases to 1000 °C, the cleavage facet grows again and the tearing edges start to turn blunt (Fig. 10e), resulting in the reduction in impact toughness compared with PT-920 °C. While for the highest PT of 1350 °C, the fracture mechanism transforms into cleavage fracture with fan-shaped river pattern (Fig. 10f). The fracture is relatively flat and no dimple is observed on the lateral tearing edges, which significantly reduces the capability of energy consumption during crack propagation, consequently leading to a much low toughness as seen in Fig. 8b. In addition, it can also be seen that the cleavage facet size for PT-1350 °C is almost twice than that of HAZs with PT of 850, 920 and 1000 °C, which to some extent commits a negative effect on the toughness.

4. Discussions

4.1. The evolutions of microstructural features during thermal simulation process

For the investigated rail steel, its initial microstructure is dominated by fine BF with some M-A constituents, AF and TM (Fig. 4a). With the introduction of simulated thermal cycles, the microstructural features present remarkable differences (Fig. 4(b–f)), suggesting that complicated phase transformation occurred during welding. In order to deepen the understanding of phase transformation involved, the dilatometry tests were carried out following the same heat treatments as the thermal simulations, and the curve comparisons are shown in Fig. 11. Fig. 11a presents the dilatometric curves of the whole thermal cycles. It is clear that the welding PT corresponding to the austenitization temperature would vary the temperature range of phase transformation during cooling. In order to clearly observe the variation, Fig. 11b gives the partial dilatometric curves with respect to the temperature range from 600 to 200 °C at the cooling rate of 0.3 °C/s. As seen, the current temperature window only presents the bainite transformation region, and no visible martensite transformation region is found which may be due to the cause of small amount of martensite formed. It is clear that no phase transformation appears for PT-700 °C due to the low PT below the Ac_1. With increasing PT, the bainite starting (B_s) temperature gradually increases. It demonstrates that a low PT (i.e., austenitization temperature) can postpone bainite transformation starts, which is opposite to the general idea that a higher austenitization temperature leading to more homogenization of microstructure and chemical composition results in a lower B_s. That could be due to the possibility that the difficulty in homogenization due to the short holding time at PT and the fine austenite grains obtained under low PT as seen in Fig. 8a can delay bainite nucleation by impeding the mobility of dislocations upon the Hall-Petch strengthening effect [45,46]. Therefore, the welding PT has a significant influence on the diffusion and distribution of solute atoms in austenite and then affects the transformation products in the following cooling stages. For a low PT (such as 700 °C) below the Ac_1, no austenitizing and subsequent bainite transformation occurs. But, the polygonization of BF, and the carbides formation by decomposition of RA as well as the formation of TM can take place instead. For PT-850 °C located between the Ac_1 and Ac_3 referring to two-phase region, the main microstructures are BF and AF, accompanied by some carbides (Fig. 5e) due to the high carbon content in austenite. While in the case of PT-920 °C (above the Ac_3), due to the relatively low B_s, the BF is mainly consisted of typical lower bainite (Fig. 5g). As the PT reaches 1000 °C, the homogenization of solute atoms is greatly improved, and the sufficient recrystallization makes austenite grain boundaries completeness which can provide more sites for bainite sheaves nucleation [47]. As a result, upon the relatively high B_s, the microstructure is consisted of wider BF lath than that in PT-920 °C, as seen in Fig. 5h. As the PT increases to 1350 °C, despite of the higher uniformity in austenite, the highest B_s is prone to lead to the formation of coarse BF and coarse M-A constitutes, as seen in Fig. 4f and Fig. 5(j-k). According to the above analysis, the microstructural evolutions of simulated HAZs subjected to different PTs can be summarized in Fig. 12.

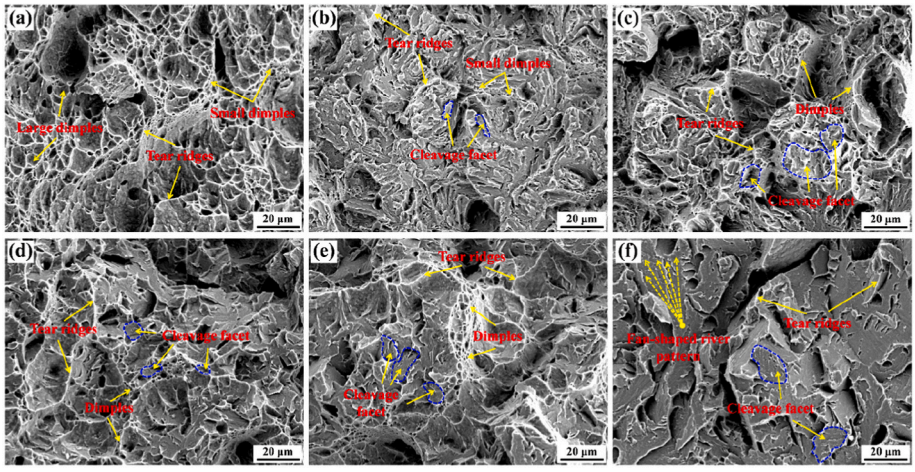

Fig. 10. Radial region morphologies of impact fractures by SEM observations: (a) BM, (b) PT-700 °C, (c) PT-850 °C, (d) PT-920 °C, (e) PT-1000 °C and (f) PT-1350 °C.

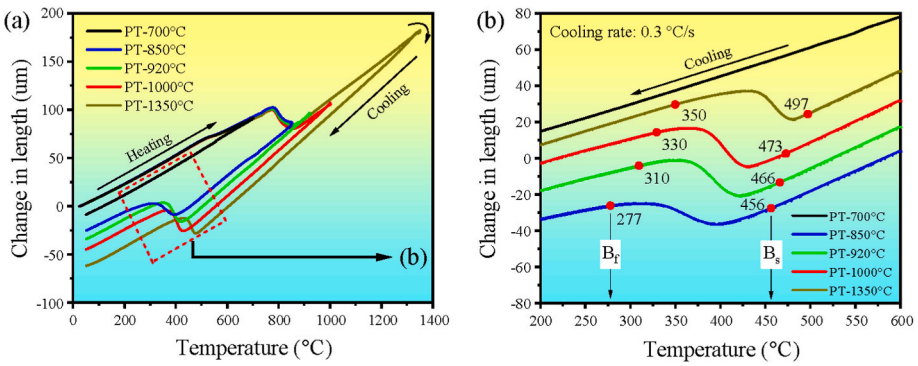

Fig. 11. Dilatometric curves for each simulated HAZ subzone sample.

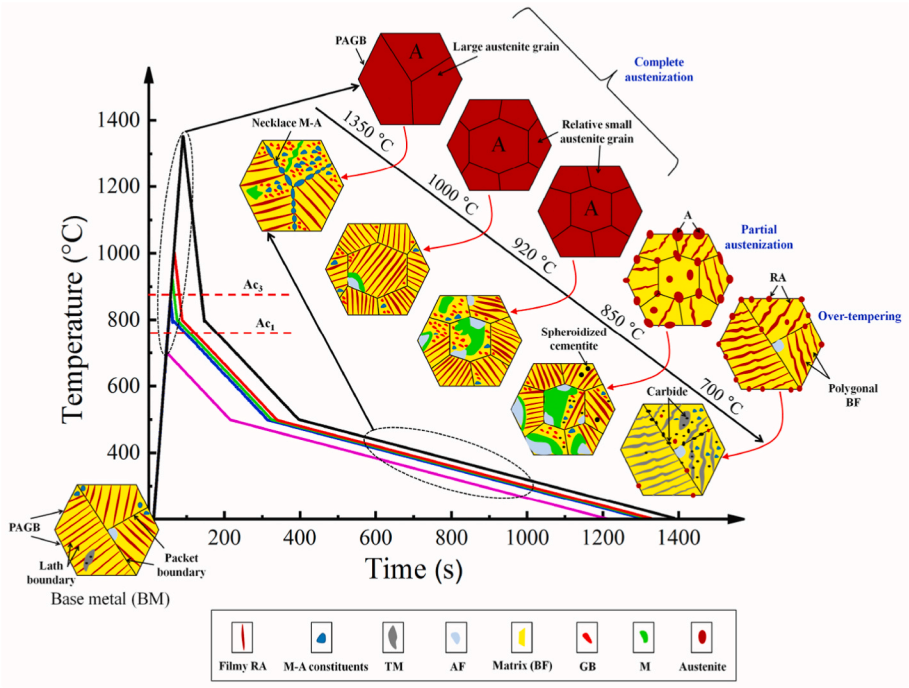

Fig. 12. Microstructural evolution diagram for simulated HAZs subjected to different PTs.

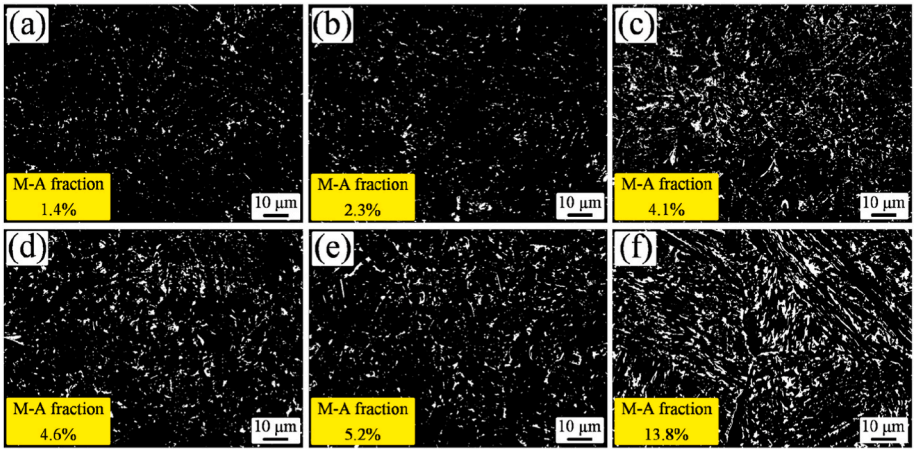

Fig. 13. Morphologies and distributions of M-A constituents (white in color) corresponding to the OM observation post-treated by IPP software: (a) BM, (b) PT-700 °C, (c) PT-850 °C, (d) PT-920 °C, (e) PT-1000 °C and (f) PT-1350 °C. (For interpretation of the references to color in this figure legend, the reader is referred to the Web version of this article.)

4.2. The effect of M-A constituents on impact toughness

In order to unravel the effect of M-A constituents on impact toughness, a series of OM images of the BM and simulated HAZs were post-treated with the aid of binary processing function in IPP software to highlight the M-A constituents on the basis of colour contrast after Lepera etching, as seen in Fig. 13. For the BM, it presents small M-A constituents with a lowest volume fraction of 1.4% (Fig. 13a). With the PT increases, the size and volume fraction of M-A constituents increases gradually (Fig. 13(b–f)). In particular for PT-1350 °C, a highest volume fraction of M-A constituents (13.8%) is observed, showing a large size with long strip and blocky structure. In order to quantify the initial volume fraction of M-A constituents with different morphologies, according to Ref. [48], (semi-) quantitative analysis on the morphology of M-A constituents have been done by dividing them into four types base on the maximum length (L_{max}) and aspect ratio (L_{max}/W_{max}, maximum length/maximum width), i.e., island-like M-A constituents (L_{max}<3 μm, aspect ratio<3), fine slender M-A constituents (L_{max}<3 μm, aspect ratio>3), blocky M-A constituents (L_{max}>3 μm, aspect ratio<3) and coarse slender M-A constituents (L_{max}>3 μm, aspect ratio>3), as statistically presented in Fig. 14. It is clear that the island-like and fine slender M-A constituents in each case is predominant and secondly, respectively. As reported in Ref. [49], the M-A constituents can play an important role in determining the impact toughness, i.e., 1) the island-like M-A constituents contribute to toughness improvement by suppressing crack propagation, while the fine slender M-A phases have weak capacity to resist crack propagation, and 2) the blocky and coarse slender M-A constituents can severely deteriorate the toughness since cracks are easily formed on the interfaces between blocky/coarse slender M-A constituents and matrix upon local stress concentration. Hence, the island-like M-A constituents mainly play a role in suppressing crack propagation and benefit to the toughness. While for PT-1350 °C, although it has a highest fraction (61.0%) of island-like M-A constituents (Fig. 14), the impact toughness is yet the lowest, which could be mainly attributed to the existence of high fraction blocky and coarse slender M-A constituents (i.e., 6.0% and 5.4%, respectively). With the decrement in PT, the percentage of not only the island and fine slender M-A constituents but also the blocky and coarse slender M-A constituents decrease, consequently leading to a trade-off in PT-920 °C where it possesses a highest impact toughness compared with the other HAZs (Fig. 8b).

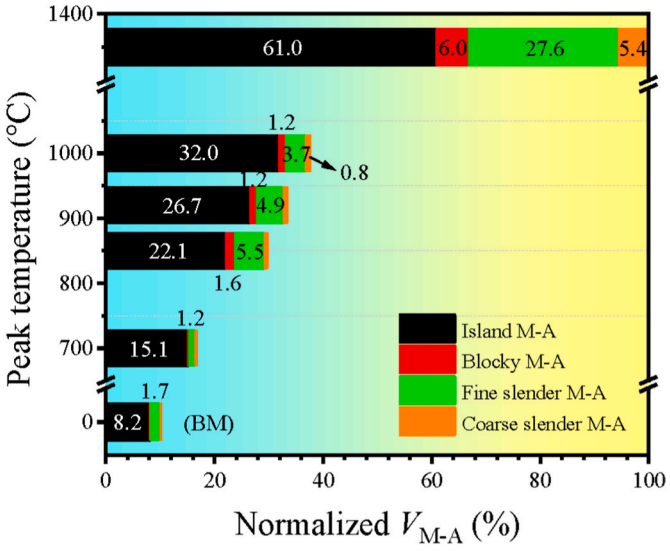

Fig. 14. Normalized volume fraction of M-A constituents in the BM and simulated HAZs.

4.3. The dependence of impact toughness on microstructural features

In order to deep analyse the impact fracture behaviors in the BM and simulated HAZs, the impact load-displacement curves and resulting impact toughness are given in Fig. 15. On the basis of instrumented Charpy impact test, the ideal curve generally involves five stages [50–52], i.e., elastic deformation stage, plastic deformation stage, ductile propagation stage, brittle propagation stage and ductile fracture stage, as shown in Fig. 15a. Accordingly, the energy consumption during the former two stages refers to the CIE, while the energy consumption during the latter three stages refers to the CPE.

For the BM, its microstructure is mainly fine BF and tiny M-A constituents, which could impart a super toughness and hence a much high CIE and CPE (Fig. 15a). In addition, the slow transition in the ductile propagation stage (P_m: maximum load → P_f: fracture load)) and brittle propagation process (P_f → P_a: crack arresting load) also suggests that the BM has a good ductile. In contrast, the simulated HAZs (Fig. 15(b–f)) have quite sharp transition of ductile and brittle propagation stages, and the impact loads decrease rapidly from P_f to P_a corresponding to unstable brittle fracture. In general, the simulated HAZs have a lower CIE and CPE than the BM. For PT-700 °C, a strong softening of the microstructures due to over-tempering (Fig. 8a) results in a low CIE referring to a short yield stage (i.e., plastic deformation stage) before the impact load reaches the P_m (Fig. 15b). Moreover, the formation of coalesced BF and carbides precipitation (Fig. 4b) as well as the recovery of dislocation substructure (Fig. 5d) can also lead to a dramatical decrease in CPE. In the case of PT-850 °C, the microstructure has a higher CIE and total absorbed energy (Fig. 15c), which may be mainly ascribed to the presence of many AF, which can improve the coordinated deformation capability of duplex microstructure as well as has certain blunting effect on microcrack tip [53], consequently enhancing the CIE and CPE. Besides, the high fraction HAGBs as shown in Fig. 7a can also improve the CPE [54], resulting in a higher toughness than that of PT-700 °C. As the PT reaches 920 °C, it presents an obvious plastic deformation stage before reaching the P_m corresponding to a highest CIE and total absorbed energy (Fig. 15d), which could be due to the cause of main lower bainite microstructures and more island M-A constituents (Fig. 14) as well as finer prior austenite grains (Fig. 8a). As the PT increases to 1000 °C, the CIE and total absorbed energy starts to decrease (Fig. 15e), which could be related to the microstructural evolutions with regarding to the reduction in HAGBs (Fig. 7a) and enlarged austenite grains (Fig. 4d), consequently resulting in the reduction in CIE and CPE. For PT-1350 °C, in contrast, there is nearly no yield stage before the impact load reaches the P_m and the impact load decreases rapidly after reaching the P_m (Fig. 15f), indicating the crack propagation is quick and the brittleness fracture mainly occurred. Combined with the microsturcture observations, the worst toughness could be the result of coarse BF, coarse M-A constituents and severely coarsened austenite grains (Fig. 4f) as well as the low-fraction HAGBs (Fig. 7a). In particular with RA of the highest volume fraction, upon impact action RA could be transformed into martensite, which may increase the brittleness, hence further reduce the CPE as well as the total toughness.

5. Conclusions

The results of systematic experimental investigations into the microstructural evolutions and impact toughness of HAZs as a function of welding peak temperatures simulated by Gleeble-3500 simulator for a high-strength carbide-free bainitic rail steel are presented. The results on the microstructural features and resulting impact toughness for the bainitic rail steel heat treated to reproduce each HAZ subzones (i.e., SCHAZ, ICHAZ, FGHAZ and CGHAZ) are discussed. The main conclusions can be summarized as following.

1) The microstructural features of simulated HAZ subzones present great differences depending on the welding PT. Compared to the BM

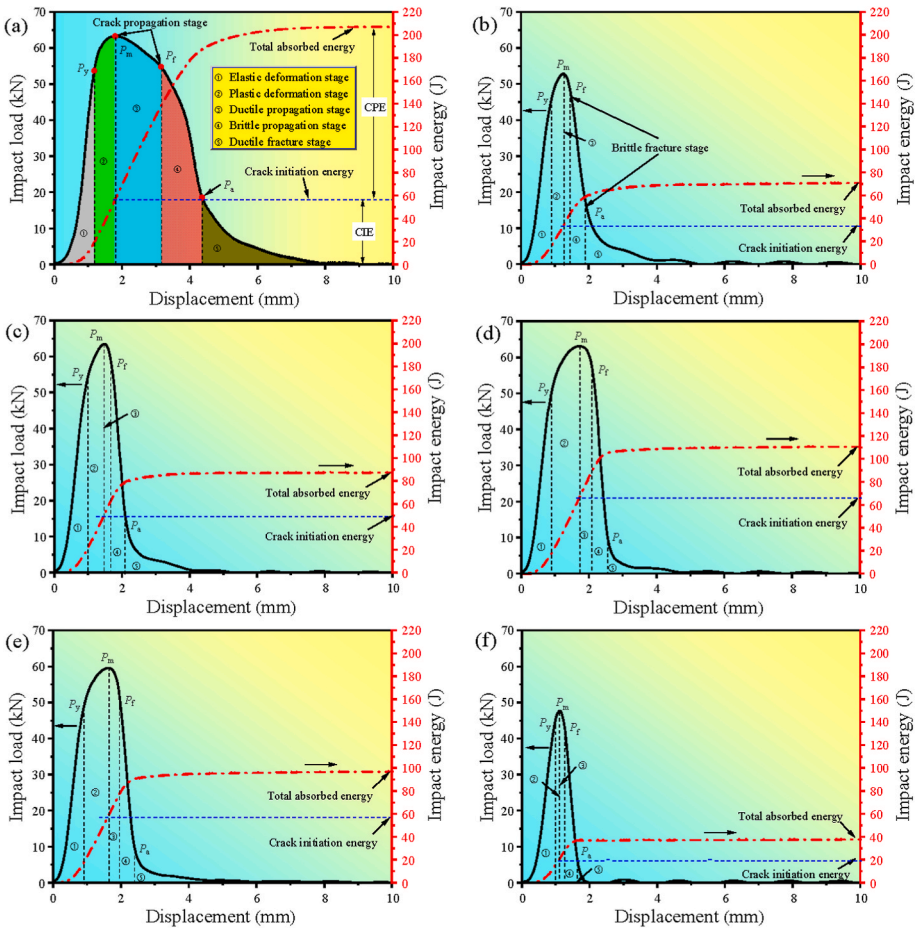

Fig. 15. Impact load-displacement and impact toughness curve: (a) BM, (b) PT-700 °C, (c) PT-850 °C, (d) PT-920 °C, (e) PT-1000 °C and (f) PT-1350 °C. Note: P_y-yield load, P_m-maximum load, P_f-fracture load, P_a-crack arresting load.

with fine BF, the dominant bainitic microstructure of HAZ subzone evolves from a polygonal BF for PT-700 °C, to a mixture of fine BF and GB for PT-850 °C ~ PT-1000 °C, and finally to coarse BF and GB for PT-1350 °C.

2) Compared to the BM, the HAZs have a much lower impact toughness. For HAZ subzones, they present a trend of firstly increase and then decrease with increasing PT. The microstructure for PT-920 °C (i.e., FGHAZ) has a best impact toughness, which could be attributed to the lower bainite, more island-like M-A constituents, high fraction HAGBs and refined prior austenite grain.
3) The impact fracture morphologies reveal that the PT-700 °C subzone shows a quasi-cleavage fracture. There is a mixed fracture modes of ductile and cleavage fracture for PT-850 °C, PT-920 °C and PT-1000 °C, while a single cleavage fracture for PT-1350 °C.
4) The morphology and distribution of M-A constituents is strongly dependent on the welding PT. The formation of high fraction blocky and coarse slender M-A constituents is a key factor that deteriorates the impact toughness in CGHAZ (PT-1350 °C).

CRediT authorship contribution statement

Xiaojun Xu: Conceptualization, Methodology, Writing - review & editing. **Yunxiao Liang:** Data curation, Methodology. **Zhenyu Han:** Formal analysis, Methodology, Resources. **Zhendong Sheng:** Formal analysis, Software, Writing - review & editing. **Minhao Zhu:** Conceptualization, Methodology, Writing - review & editing.

Declaration of competing interest

The authors declare that they have no known competing conflict interests or personal relationships that could have appeared to influence the work reported in this paper.

Data availability

Data will be made available on request.

Acknowledgements

The authors gratefully acknowledge financial supported by Natural Science Foundation of China (NO. 52171079), and Science and Technology Program of Sichuan Province, China (NO. 2023NSFSC0413 and NO. 2020ZDZX0011).

References

[1] R.O. Olivares, C.I. Garcia, A. DeArdo, S. Kalay, R.F.C. Hernández, Advanced metallurgical alloy design and thermomechanical processing for rails steels for North American heavy haul use, Wear 271 (2011) 364–373.
[2] S.S. Sahay, G. Mohapatra, G.E. Totten, Overview of pearlitic rail steel: accelerated cooling, quenching, microstructure, and mechanical properties, J. ASTM Int. (JAI) 6 (2009) 1–26.
[3] M. Masoumi, G. Tressia, D.M.A. Centeno, H. Goldenstein, Improving the mechanical properties and wear resistance of a commercial pearlitic rail steel using a two-step heat treatment, Metall. Mater. Trans. A 52 (2021) 4888–4906.
[4] T. Kimura, M. Takemasa, M. Honjo, Development of SP3 rail with high wear resistance and rolling contact fatigue resistance for heavy haul railways, Tech. rep., JFE steel 26 (2010) 11–16.

[5] SP4 rail information stems from the product brochure of JFE Steel Corporation. https://www.jfe-steel.co.jp/en/products/shapes/catalog/d1e-001.pdf.
[6] E. Magel, P. Mutton, A. Ekberg, A. Kapoor, Rolling contact fatigue, wear and broken rail derailments, Wear 366–367 (2016) 249–257.
[7] E.V. Polevoi, G.N. Yunin, M.V. Temlyantsev, Differential heat treatment of rails by means of rolling heat, Steel Transl. 46 (2016) 692–700.
[8] M. Masoumi, E.A.A. Echeverri, A.P. Tschiptschin, H. Goldenstein, Improvement of wear resistance in a pearlitic rail steel via quenching and partitioning processing, Sci. Rep. 9 (2019) 7454.
[9] H. Yokoyama, S. Mitao, S. Yamamoto, M. Fujikake, Effect of the angle of attack on flaking behavior in pearlitic and bainitic steel rails, Wear 253 (2002) 60–66.
[10] M.N. Georgiev, T.V. Simeonova, Railroad rails from bainitic steel, Met. Sci. Heat Treat. 60 (2018) 464–470.
[11] S.M. Hasan, M. Ghosh, D. Chakrabarti, S.B. Singh, Development of continuously cooled low-carbon, low-alloy, high strength carbide-free bainitic rail steels, Mater. Sci. Eng., A 771 (2020), 138590.
[12] S.M. Hasan, D. Chakrabarti, S.B. Singh, Dry rolling/sliding wear behaviour of pearlitic rail and newly developed carbide-free bainitic rail steels, Wear 408–409 (2018) 151–159.
[13] Y.D. Chen, R.M. Ren, X.J. Zhao, C.H. Chen, R. Pan, Study on the surface microstructure evolution and wear property of bainitic rail steel under dry sliding wear, Wear 448–449 (2020), 203217.
[14] Y. Hu, L.C. Guo, M. Maiorino, J.P. Liu, H.H. Ding, R. Lewis, E. Meli, A. Rindi, Q. Y. Liu, W.J. Wang, Comparison of wear and rolling contact fatigue behaviours of bainitic and pearlitic rails under various rolling-sliding conditions, Wear 460–461 (2020), 203455.
[15] S.P. Neog, S.D. Bakshi, S. Das, Microstructural evolution of novel continuously cooled carbide free bainitic steel during sliding wear, Wear 456–457 (2020), 203359.
[16] X. Xu, Z.Y. Wang, G.H. Gao, X. Zhang, G.Z. Kang, Q.H. Kan, The effect of microstructure evolution on the ratchetting-fatigue interaction of carbide-free bainite rail steels under different heat-treatment conditions, Int. J. Fatig. 160 (2022), 106872.
[17] W.J. Hui, Z.B. Xu, Y.J. Zhang, X.L. Zhao, C.W. Shao, Y.Q. Weng, Hydrogen embrittlement behavior of high strength rail steels: a comparison between pearlitic and bainitic microstructures, Mater. Sci. Eng., A 704 (2017) 199–206.
[18] Y.J. Zhang, Z.B. Xu, X.L. Zhao, G.H. Gao, W.J. Hui, Y.Q. Weng, Hydrogen embrittlement behavior of high strength bainitic rail steel: effect of tempering treatment, Eng. Fail. Anal. 93 (2018) 100–110.
[19] J.Z. Zhao, X. Pang, P.L. Fu, Y. Wang, G.Z. Kang, P. Wang, Q.H. Kan, Dynamic constitutive model of U75VG rail flash-butt welded joint and its application in wheel-rail transient rolling contact simulation, Eng. Fail. Anal. 134 (2022), 106078.
[20] T.A. Patel, V. Badheka, Rail Welding Technology: Processes and Welding Quality, Recent Adv. Mech. Infrastructure, Springer, 2022, pp. 369–381, https://doi.org/10.1007/978-981-16-7660-4_33.
[21] Y. Liu, K.S. Tsang, E.T. Zhi'En, N.A. Subramaniam, J.H.L. Pang, Investigation on material characteristics and fatigue crack behavior of thermite welded rail joint, Construct. Build. Mater. 276 (2021), 122249.
[22] M. Ghazanfari, P.H. Tehrani, Experimental and numerical investigation of the characteristics of flash-butt joints used in continuously welded rails, Proc. Inst. Mech. Eng. F J. Rail Rapid Transit 234 (2020) 65–79.
[23] X.H. Yu, J.L. Caron, S.S. Babu, J.C. Lippold, D. Isheim, D.N. Seidman, Characterization of microstructural strengthening in the heat-affected zone of a blast-resistant naval steel, Acta Mater. 58 (2010) 5596–5609.
[24] Y. Zhang, J. Xiao, W. Liu, A.M. Zhao, Effect of welding peak temperature on microstructure and impact toughness of heat-affected zone of Q690 high strength bridge steel, Materials 14 (2021) 2981.
[25] X.J. Di, M. Tong, C.N. Li, C. Zhao, D.P. Wang, Microstructural evolution and its influence on toughness in simulated inter-critical heat affected zone of large thickness bainitic steel, Mater. Sci. Eng., A 743 (2019) 67–76.
[26] X.D. Li, X.P. Ma, S.V. Subramanian, C.J. Shang, R.D.K. Misra, Influence of prior austenite grain size on martensite-austenite constituent and toughness in the heat affected zone of 700 MPa high strength linepipe steel, Mater. Sci. Eng., A 616 (2014) 141–147.
[27] J. Hu, L.X. Du, H. Xie, F.T. Dong, R.D.K. Misra, Effect of weld peak temperature on the microstructure, hardness, and transformation kinetics of simulated heat affected zone of hot rolled ultra-low carbon high strength Ti-Mo ferritic steel, Mater. Des. 60 (2014) 302–309.
[28] M.C.G. Rios, J.D.C. Payão Filho, F.W.C. Farias, A.V. Passos, V.H.P. Moraes E Oliveira, Microstructural characterization of the physical simulated and welded heat-affected zone of 9% Ni steel pipe, J. Mater. Res. Technol. 17 (2022) 3033–3046.
[29] K. Poorhaydari, B.M. Patchett, D.G. Ivey, Estimation of cooling rate in the welding of plates with intermediate thickness, Weld. J. 84 (2005) 149–155. http://files.aws.org/wj/supplement/WJ_2005_10_s149.pdf.
[30] D.S. Mei, Pangang Rail Production System Innovation and New Products Development, Adv. Steels, 2011, pp. 501–507, https://doi.org/10.1007/978-3-642-17665-4_50.
[31] A. Królicka, K. Radwański, R. Kuziak, T. Zygmunt, A. Ambroziak, Microstructure-based approach to the evaluation of welded joints of bainitic rails designed for high-speed railways, J. Constr. Steel Res. 175 (2020), 106372.
[32] K.K. Wang, Z.L. Tan, G.H. Gao, X.L. Gui, R.D.K. Misra, B.Z. Bai, Ultrahigh strength-toughness combination in bainitic rail steel: the determining role of austenite stability during tempering, Mater. Sci. Eng., A 662 (2016) 162–168.
[33] D.W. Suh, S.J. Park, T.H. Lee, C.S. Oh, S.J. Kim, Influence of Al on the microstructural evolution and mechanical behavior of low-carbon, manganese transformation-induced-plasticity steel, Metall. Mater. Trans. 41 (2010) 397–408.
[34] X.N. Wang, Y.J. Zhao, P.F. Guo, X.N. Qi, H.S. Di, M. Zhang, C.J. Chen, Effect of heat input on M-A constituent and toughness of coarse grain heat-affected zone in an X100 pipeline steel, J. Mater. Eng. Perform. 28 (2019) 1810–1821.
[35] K. Srivatsa, P. Srinivas, G. Balachandran, V. Balasubramanian, Room temperature microstructure and property evaluation of a heat treated fully bainitic 20CrMoVTiB410 steel, JOM (J. Occup. Med.) 68 (2016) 2704–2712.
[36] Z.H. Jiang, Y.H. Li, Z.D. Yang, P. Wang, D.Z. Li, Y.Y. Li, The tempering behavior of martensite/austenite islands on the mechanical properties of a low alloy Mn-Ni-Mo steel with granular bainite, Mater. Today Commun. 26 (2021), 102166.
[37] Z.Y. Liu, Q.Z. Gao, H.L. Zhang, S.H. Luo, X. Zhang, W. Li, Y.J. Jiang, H.J. Li, EBSD analysis and mechanical properties of alumina-forming austenitic steel during hot deformation and annealing, Mater. Sci. Eng., A 755 (2019) 106–115.
[38] L.Y. Zhao, Q.M. Wang, G.H. Shi, B. Hu, S.B. Wang, M.L. Qiao, Q.F. Wang, R.P. Liu, The impacts of M/A constituents decomposition and complex precipitation on mechanical properties of high-strength weathering steel subjected to tempering treatment, J. Mater. Res. Technol. 23 (2023) 2504–2526.
[39] E.A. Ariza-Echeverri, M. Masoumi, A.S. Nishikawa, D.H. Mesa, A.E. Marquez-Rossy, A.P. Tschiptschin, Development of a new generation of quench and partitioning steels: influence of processing parameters on texture, nanoindentation, and mechanical properties, Mater. Des. 186 (2020), 108329.
[40] M. Wallner, K. Steineder, R. Schneider, C. Commendac, C. Sommitsch, Effect of galvannealing on the microstructural and mechanical properties of a Si and Al alloyed medium-Mn quenching and partitioning steels, Mater. Sci. Eng., A 841 (2022), 143067.
[41] Y. You, C.J. Shang, W.J. Nie, S. Subramanian, Investigation on the microstructure and toughness of coarse grained heat affected zone in X-100 multi-phase pipeline steel with high Nb content, Mater. Sci. Eng., A 558 (2012) 692–701.
[42] X.L. Wang, Z.Q. Wang, X.P. Ma, S.V. Subramanian, Z.J. Xie, C.J. Shang, X.C. Li, Analysis of impact toughness scatter in simulated coarse-grained HAZ of E550 grade offshore engineering steel from the aspect of crystallographic structure, Mater. Char. 140 (2018) 312–319.
[43] H. Kitahara, R. Ueji, N. Tsuji, Y. Minamino, Crystallographic features of lath martensite in low-carbon steel, Acta Mater. 54 (2006) 1279–1288.
[44] D. Kumar, S. Idapalapati, W. Wang, S. Narasimalu, Effect of surface mechanical treatments on the microstructure-property-performance of engineering alloys, Materials 12 (2019) 2503.
[45] S.J. Lee, J.S. Park, Y.K. Lee, Effect of austenite grain size on the transformation kinetics of upper and lower bainite in a low-alloy steel, Scripta Mater. 59 (2008) 87–90.
[46] L.Y. Lan, C.L. Qiu, D.W. Zhao, X.H. Gao, L.X. Du, Effect of reheat temperature on continuous cooling bainite transformation behavior in low carbon microalloyed steel, J. Mater. Sci. 48 (2013) 4356–4364.
[47] A. Matsuzaki, H.K.D.H. Bhadeshia, Effect of austenite grain size and bainite morphology on overall kinetics of bainite transformation in steels, Mater. Sci. Technol. 15 (1999) 518–522.
[48] R.H. Duan, G.M. Xie, P. Xue, Z.Y. Ma, Z.A. Luo, C. Wang, R.D.K. Misra, G.D. Wang, Microstructural refinement mechanism and its effect on toughness in the nugget zone of high-strength pipeline steel by friction stir welding, J. Mater. Sci. Technol. 93 (2021) 221–231.
[49] X.C. Yang, X.J. Di, X.G. Liu, D.P. Wang, C.N. Li, Effects of heat input on microstructure and fracture toughness of simulated coarse-grained heat affected zone for HSLA steels, Mater. Char. 155 (2019), 109818.
[50] X. Luo, X.H. Chen, T. Wang, S.W. Pan, Z.D. Wang, Effect of morphologies of martensite-austenite constituents on impact toughness in intercritically reheated coarse-grained heat-affected zone of HSLA steel, Mater. Sci. Eng., A 710 (2018) 192–199.
[51] X.G. Li, Z.P. Cai, M.J. Hu, K.J. Li, M.D. Hou, J.L. Pan, Effect of NbC precipitation on toughness of X12CrMoWNbVN10-1-1 martensitic heat resistant steel for steam turbine blade, J. Mater. Res. Technol. 11 (2021) 2092–2105.
[52] L.Y. Lan, C.L. Qiu, L.X. Du, Effective grain size dependence of crack propagation resistance in low carbon steel, Theor. Appl. Fract. Mech. 124 (2023), 103762.
[53] P.G. Xu, H.S. Fang, B.Z. Bai, Z.G. Yang, Toughness of grain boundary allotriomorphic ferrite/granular bainite duplex microstructure, Acta Metall. Sin. 38 (2002) 255–260. https://www.ams.org.cn/CN/Y2002/V38/I3/255.
[54] X.N. Qi, P.C. Huan, X.N. Wang, Z.G. Liu, X.J. Shen, Y. Gao, H.S. Di, Effect of root welding heat input on microstructure evolution and fracture mechanism in intercritically reheat-coarse grained heat-affected zone of X80 pipeline steel, Mater. Today Commun. 31 (2022), 103413.